JOC Article

Chiral Recognition of Peptide Enantiomers by Cinchona Alkaloid Derived Chiral Selectors: Mechanistic Investigations by Liquid Chromatography, NMR Spectroscopy, and Molecular Modeling

Christoph Czerwenka,[†] Mei Mei Zhang,[‡] Hanspeter Kählig,[§] Norbert M. Maier,[†] Kenny B. Lipkowitz,[‡] and Wolfgang Lindner*[,†]

Institute of Analytical Chemistry, University of Vienna, Währingerstrasse 38, 1090 Wien, Austria, Department of Chemistry, North Dakota State University, Fargo, North Dakota 58105, and Institute of Organic Chemistry, University of Vienna, Währingerstrasse 38, 1090 Wien, Austria

wolfgang.lindner@univie.ac.at.

Received May 22, 2003

The chiral recognition mechanism of a cinchona alkaloid based chiral selector for *N*-protected peptide enantiomers was investigated. A chiral stationary phase derived from this selector was employed for liquid chromatographic enantiomer separations. It showed exceptionally high enantiomer discrimination for the (*all-R*)- and (*all-S*)-enantiomers of dialanine ($\alpha = 20$), while a pronounced loss of chiral recognition occurred upon the insertion of an additional alanine residue into the peptide backbone. This reduction of enantioselectivity was investigated in great detail by NMR spectroscopy of complexes of the chiral selector and the analyte enantiomers accompanied by molecular modeling studies. Investigation of intramolecular NOEs provided the conformational states of the free and complexed forms of the selector. The analysis of complexation-induced shifts yielded information on intermolecular interactions and allowed us to propose binding models, which were further supported by the observation of intermolecular NOEs, indicating the relative arrangements of selector and analytes. Stochastic molecular dynamics simulations were able to reproduce the chromatographic retention orders and energy differences, as well as the intermolecular NOEs. The computational data were used to evaluate the intermolecular forces responsible for analyte binding. In addition, the relative contributions of the fragments of the chiral selector to the enantioselective binding event were assessed. A spatial arrangement of the chiral selector and the analyte allowing the primary ionic interaction as well as hydrogen bonding and $\pi-\pi$-stacking to take place simultaneously was found to be essential to obtain very high enantioselectivities.

1. Introduction

The direct chromatographic separation of enantiomers is of great importance in a variety of fields including the pharmaceutical, agro, and fine chemicals industry, both at analytical and preparative scale.[1] For chromatographic enantiomer separations a wide array of chiral selectors are available; however, the choice of a selector suited for a specific separation problem often relies on a trial-and-error approach due to the lack of extensive understanding of the underlying discrimination mechanisms. Therefore, advancing the knowledge on the stereoselective recognition mechanism of chiral selectors is not only of interest from an academic point of view but also of importance for practical reasons. These include the choice of a suitable selector for a given analyte ("selectand") and the development of new and refinement of existing selectors, as well as for broadening their scope of application or tailoring "receptor-like" selectors aimed at the specific target of a single (group of) molecule(s). Further, a well-understood chiral recognition mechanism can, in some cases, allow the indirect assignment of the absolute configuration of an analyte of unknown stereochemistry.

Unfortunately, the polymeric nature and supramolecular complexity of many of the widely used natural chiral selectors (e.g. polysaccharides, antibiotics, or proteins) make studies targeted at the elucidation of stereoselective molecular recognition mechanisms difficult. In contrast, low molecular weight synthetic selectors facilitate the investigation of stereoselective binding phenomena.

Cinchona alkaloid derivatives, e.g., carbamoylated quinine, represent one group of the large array of synthetic selectors available nowadays. These chiral selectors have been successfully employed for enantiomer separations of acidic analytes with use of liquid chromatography,[2−5] capillary electrophoresis,[6−8] and capillary electrochromatography.[9−11]

* Corresponding author. Phone: +43 1 4277 52300. Fax: +43 1 4277 9523.
[†] Institute of Analytical Chemistry, University of Vienna.
[‡] North Dakota State University.
[§] Institute of Organic Chemistry, University of Vienna.

(1) Maier, N. M.; Franco, P.; Lindner, W. *J. Chromatogr. A* **2001**, *906*, 3−33.
(2) Lämmerhofer, M.; Lindner, W. *J. Chromatogr. A* **1996**, *741*, 33−48.
(3) Maier, N. M.; Nicoletti, L.; Lämmerhofer, M.; Lindner, W. *Chirality* **1999**, *11*, 522−528.
(4) Mandl, A.; Nicoletti, L.; Lämmerhofer, M.; Lindner, W. *J. Chromatogr. A* **1999**, *858*, 1−11.

10.1021/jo0346914 CCC: $25.00
Published on Web 10/02/2003

In a recent paper reporting high-performance liquid chromatography (HPLC) enantiomer separation of *N*-acylated oligopeptides on chiral stationary phases based on these cinchona alkaloid derivatives,[5] a particular behavior of enantioselectivity in terms of chain length was described. A very pronounced drop in enantioselectivity was observed for the separation of 3,5-dinitrobenzoylated peptide enantiomers between the dipeptide and the tripeptide. As the elution order remained unchanged and only a slight decrease in enantiomer discrimination was noted when studying tetramers and further elongated peptides, it can be assumed that the general chiral recognition remained the same. However, a loss of one (or more) stereoselective binding increment(s) was anticipated to occur that effected the large loss of enantiomeric discrimination. To investigate this phenomenon and to enhance the knowledge on the underlying molecular recognition mechanism a detailed NMR study was carried out to elucidate the factors responsible for these observations. In addition, molecular modeling was employed to study the intermolecular forces responsible for chiral recognition from a theoretical point of view.

In this contribution we thus present the enhanced insights into the chiral recognition mechanism of one representative of the family of cinchona alkaloid derived chiral selectors for peptide enantiomers based on the results of our experimental and theoretical studies. Specifically, the exceptional chiral recognition capabilities of 6′-neopentoxy-9-*O*-*tert*-butylcarbamoylcinchonidine (Figure 1, **SO1**) for 3,5-dinitrobenzoyl dialanine (HPLC: $\alpha \approx 20$)[5] versus those for the significantly less well resolved 3,5-dinitrobenzoyl trialanine (Figure 1, **SA1** and **SA2**, respectively) are investigated in detail.

2. Results and Discussion

2.1. Chromatographic Determination of Enantioselectivities and Differential Free Binding Energies. For HPLC enantiomer separations, an immobilized version of the chiral selector was used. The chromatographic enantioselectivities (α), which are defined as the ratio of the retention factors of the two enantiomers k_R and k_S, can be used to calculate the differential free binding energies according to $\Delta_{S/R}(\Delta G) = -RT\cdot\ln \alpha$ ($k_S > k_R$). If the nonselective retention increments are negligible compared to the enantioselective ones and immobilization of the chiral selector does not influence its enantiodiscrimination capabilities, the chromatographically determined $\Delta_{S/R}(\Delta G)$ values represent a good estimate for the intrinsic (thermodynamic) enantioselectivities. In a recent study these conditions were found to be fulfilled for the present selector and a selectand closely related to the investigated peptide analytes, thus enabling the above-mentioned deductions.[12]

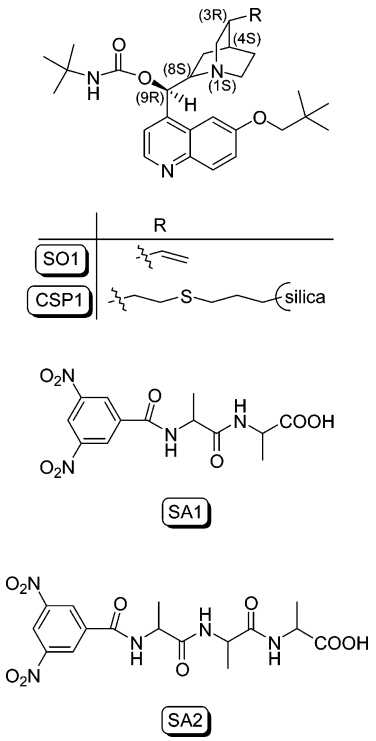

FIGURE 1. Structures of chiral selector (**SO1**), the related chiral stationary phase (**CSP1**), and peptide analytes (selectands **SA1** and **SA2**; being of either (*all-R*) or (*all-S*) configuration) studied.

TABLE 1. HPLC Enantiomer Separation Results on 6′-Neopentoxy-9-*O*-*tert*-butylcarbamoylcinchonidine-Based CSP[a]

sample	k_1	α	R_S	$\Delta\Delta G$ (kJ·mol^{-1})	elution order[b]
DNB-Ala	1.52	15.83	22.83	−6.85	(*S*)
DNB-Ala$_2$	1.14	19.96	20.68	−7.42	(*S*,*S*)
DNB-Ala$_3$	0.83	2.84	8.41	−2.59	(*S*,*S*,*S*)

[a] Conditions: mobile phase, 80/20 methanol/0.5 M aqueous ammonium acetate, adjusted to pH_a 6.0 with acetic acid; flow rate, 1 mL·min^{-1}; 25 °C; UV detection at 254 nm. [b] Indicating the configuration of the longer retained enantiomer.

To determine the α- and $\Delta_{S/R}(\Delta G)$ values of the (*all-R*)- and (*all-S*)-enantiomers of di- and trialanine peptides, **SO1** was immobilized to a mercaptopropyl modified silica support yielding **CSP1** (Figure 1), which was then packed into an HPLC column. Enantiomer separations of the *N*-protected peptide enantiomers (for comparison reasons the corresponding amino acid enantiomers, 3,5-dinitrobenzoyl (*R*)- and (*S*)-alanine, were also included) were performed with a buffered hydro-organic mobile phase. The observed enantioselectivities and the differential free binding energies calculated thereof are presented in Table 1. Very high enantioselectivities were achieved for the amino acid and dipeptide derivatives, whereas a significant drop in enantioselectivity (from almost 20 to below 3) was observed for the *N*-protected tripeptide. This translates into a loss of differential free binding energy

(5) Czerwenka, C.; Lämmerhofer, M.; Maier, N. M.; Rissanen, K.; Lindner, W. *Anal. Chem.* **2002**, *74*, 5658−5666.
(6) Piette, V.; Lämmerhofer, M.; Lindner, W.; Crommen, J. *Chirality* **1999**, *11*, 622−630.
(7) Lämmerhofer, M.; Zarbl, E.; Lindner, W.; Simov, B. P.; Hammerschmidt, F. *Electrophoresis* **2001**, *22*, 1182−1187.
(8) Czerwenka, C.; Lämmerhofer, M.; Lindner, W. *Electrophoresis* **2002**, *23*, 1887−1899.
(9) Lämmerhofer, M.; Lindner, W. *J. Chromatogr. A* **1998**, *829*, 115−125.
(10) Tobler, E.; Lämmerhofer, M.; Lindner, W. *J. Chromatogr. A* **2000**, *875*, 341−352.
(11) Lämmerhofer, M.; Peters, E. C.; Yu, C.; Svec, F.; Fréchet, J. M. J.; Lindner, W. *Anal. Chem.* **2000**, *72*, 4623−4628.
(12) Maier, N. M.; Schefzick, S.; Lombardo, G. M.; Feliz, M.; Rissanen, K.; Lindner, W.; Lipkowitz, K. B. *J. Am. Chem. Soc.* **2002**, *124*, 8611−8629.

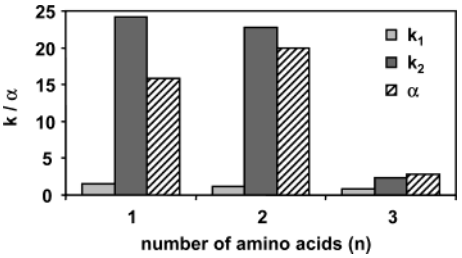

FIGURE 2. Change of retention factors and enantioselectivity in HPLC with increasing peptide length. Conditions: mobile phase, 80/20 methanol/0.5 M aqueous ammonium acetate, adjusted to pH_a 6.0 with acetic acid; flow rate, 1 mL·min^{-1}; 25 °C; UV detection at 254 nm.

of almost −4.9 kJ·mol^{-1}. From Figure 2 it becomes clear that this loss of enantioselectivity is mainly caused by a strongly reduced retention of the more strongly bound, i.e., the second eluted, enantiomer. This observation suggests a loss or at least a strong reduction of complex-stabilizing binding increments within the association structure of the (*all-S*)-tripeptide enantiomer and the chiral selector relative to that of the dipeptide.

2.2. NMR Spectroscopy. Low substance requirements, the possibility for solution-phase studies, the intrinsic sensitivity, etc. make ^{1}H NMR spectroscopy an ideal tool to elucidate these changes of binding increments. NMR spectroscopy has been shown to be a powerful tool for studying enantioselective associations between a chiral selector and the analyte enantiomers in solution in various cases. For peptide enantiomer analytes investigations employing modified cyclodextrins as chiral selectors have been reported.[13,14] Conversely, the use of peptides as chiral selectors has also been studied by NMR spectroscopy.[15−17] In several studies the insights into the chiral recognition mechanisms gained by NMR spectroscopy have served to interpret observations made during enantiomer separation experiments.[12,14,16−20]

To study the (noncovalent) binding properties of the transient diastereomeric complexes of **SO1** and the enantiomers of **SA1** and **SA2**, respectively, a combination of several 1D and 2D NMR experiments were carried out. First, the stoichiometry of the complexes was determined by continuous variation-type titration experiments. Information on the conformational preferences of the chiral selector and their changes upon complexation was extracted by analysis of intramolecular NOEs found in NOESY spectra. Further, complexation-induced shifts of both the selector's and the selectand's protons upon enantioselective binding were assessed to identify specific intermolecular interactions. Finally, intermolecular NOEs were studied to gain information on the time-averaged geometry of the complexes. To generate medium conditions similar to those used in the chromatographic experiments all experiments were carried out in methanol-

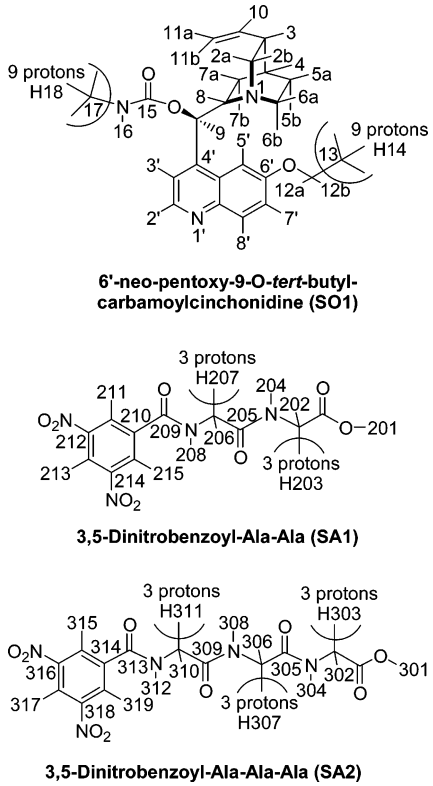

FIGURE 3. Proton numbering scheme for the studied selector and selectands.

d_4. In the following discussions the individual protons of **SO1**, **SA1**, and **SA2** are referred to according to the numbering scheme shown in Figure 3.

2.3. Complexation Stoichiometry. The knowledge of the complexation stoichiometry is a prerequisite for investigations on the molecular recognition process. Thus, the stoichiometry of the complexation of **SO1** with the more strongly bound (*all-S*)-enantiomers of **SA1** and **SA2**, respectively, was determined by a continuous variation NMR titration protocol.[21] The chemical shifts of the proton H_9 of **SO1** were measured for different molar ratios of the chiral selector and the selectands. The thus acquired Job plots (available as Supporting Information) showed a maximum at molfractions of 0.5 for both (*all-S*)-**SA1** and (*all-S*)-**SA2**, which indicates a 1:1 stoichiometry of the complexes. The ion-pair-type binding of the chiral selector and the selectands seems to occur only at the stronger basic quinuclidine nitrogen of **SO1**.

In a previous study,[12] in which the complexation of **SO1** with the enantiomers of the related *N*-3,5-dinitrobenzoylleucine was studied, the same complexation stoichiometry of 1:1 was established for both enantiomers. It was expected that the same stoichiometry be present for both enantiomers of the two peptide analytes. Therefore, only the complexation stoichiometries of the stronger binding enantiomers of the two peptides were probed.

(13) Kano, K.; Hasegawa, H.; Miyamura, M. *Chirality* **2001**, *13*, 474−482.
(14) Sü*β*, F.; Kahle, C.; Holzgrabe, U.; Scriba, G. K. E. *Electrophoresis* **2002**, *23*, 1301−1307.
(15) McEwen, I. *Biopolymers* **1993**, *33*, 933−942.
(16) De Lorenzi, E.; Massolini, G.; Molinari, P.; Galbusera, C.; Longhi, R.; Marinzi, C.; Consonni, R.; Chiari, M. *Electrophoresis* **2001**, *22*, 1373−1384.
(17) Marinzi, C.; Longhi, R.; Chiari, M.; Consonni, R. *Electrophoresis* **2001**, *22*, 3257−3262.
(18) Tárkányi, G. *J. Chromatogr. A* **2002**, *961*, 257−276.
(19) Yamamoto, C.; Yashima, E.; Okamoto, Y. *J. Am. Chem. Soc.* **2002**, *124*, 12583−12589.
(20) Zhou, L.; Thompson, R.; Reamer, R. A.; Miller, C.; Welch, C.; Ellison, D. K.; Wyvratt, J. M. *J. Chromatogr. A* **2003**, *987*, 409−420.
(21) Homer, J.; Perry, M. C. *J. Chem. Soc., Faraday Trans. 1* **1986**, *82*, 533−543.

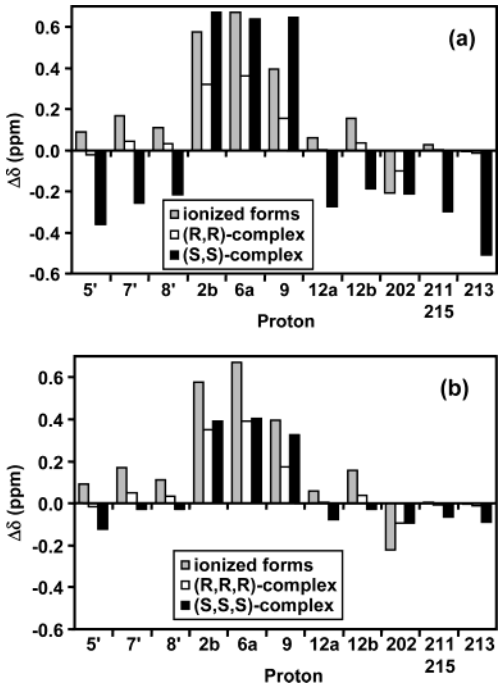

FIGURE 4. Difference of complexation-induced ^{1}H NMR shifts for selected protons (for numbering see Figure 3) of the 1:1 complexes of 6′-neopentoxy-9-*O*-*tert*-butylcarbamoylcinchonidine with the (*all*-*R*)- and (*all*-*S*)-enantiomers of (a) DNB-Ala$_2$ and (b) DNB-Ala$_3$ (the shifts are reported relative to the free forms). Spectra acquired in methanol-d_4.

2.4. Conformations of the Selector in Its Free, Protonated, and Complexed Forms. The conformational state of the chiral selector is of great importance for its enantiodiscriminating properties, as the relative arrangement of its structural features defines the dimension as well as functionalities of the enantioselective binding site. Consequently, the conformational behavior of the basic **SO1** was investigated in detail, also considering potential conformational changes induced upon complexation with the acidic analyte enantiomers.

Prior investigations have identified ionic attraction as the primary interaction force during the complexation of the selector and the selectands,[2,3] which guides the two components toward each other before other interactions come into effect. Therefore, the conformations of **SO1** were studied for its free form, the protonated state (resembling an intermediate state of the complexation process), and in the presence of the analytes. A detailed description of the conformations of the free base (**SO1**) and the protonated form (**SO1·HCl**) has been published recently.[12] Three possible conformations of the chiral selector were established: an anti-open one, in which the lone pair of the quinuclidine nitrogen points away from the quinoline ring (see also Figure 5), and two closed ones (syn and anti, depending on the orientation of the carbamoyl residue relative to the 6′-residue), in which the lone pair is directed toward the aromatic ring. The relative populations of these conformational states were assessed by the presence/absence of inter-ring NOEs between the quinoline and quinuclidine protons and the magnitude of the $^3J_{H8H9}$ coupling constant.[12]

For **SO1** all three conformations were found with an approximate open/closed ratio of 63/37. For the protonated form, **SO1·HCl**, NOEs characteristic for the anti-open conformation were found, though only one very weak cross-peak for the syn-closed state. The value of the coupling constant also indicated the practically exclusive presence of the anti-open conformation. These results show that the protonation of **SO1** significantly changes its conformational status. The complexes of the more strongly bound (*all*-*S*)-enantiomers of **SA1** and **SA2**, respectively, with **SO1** showed a similar picture to the one established for **SO1·HCl**. Several strong NOEs characteristic for the anti-open conformation were found, the presence of which was supported by a vanishing $^3J_{H8H9}$. However, one pronounced cross-peak characteristic for the anti-closed conformation was also found. These findings may be rationalized by a hybrid conformation combining properties of both the anti-open and anti-closed conformers. It seems that the complete association of **SO1** with the more strongly bound analyte enantiomers, which includes not only a long-range ion-pairing event but also short-range interactions (hydrogen-bonding, $\pi-\pi$-stacking, and steric interactions[5]), induces this conformation that does differ somewhat from the solely protonated chiral selector. For the complexes of the less strongly bound (*all*-*R*)-enantiomers of **SA1** and **SA2**, respectively, with **SO1**, NOE cross-peaks significant for all three conformations were observed. The magnitude of the $^3J_{H8H9}$ coupling constant indicated open/closed ratios of 79/21 and 90/10 for the **SA1** and **SA2** complexes, respectively. Therefore, the conformational states of these two complexes can be regarded as intermediates between those of the free (nonprotonated) selector and its complexes with the corresponding (*all*-*S*)-enantiomers.

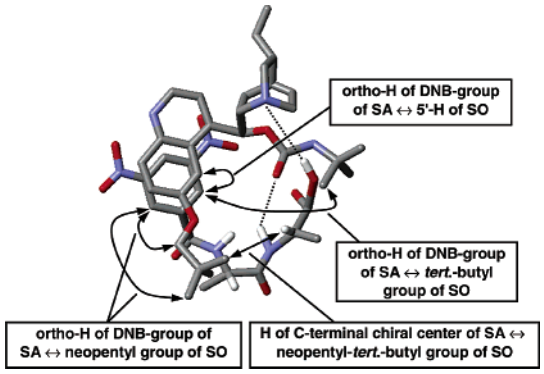

FIGURE 5. Intermolecular NOEs observed for the 1:1 complex of 6′-neopentoxy-9-*O*-*tert*-butylcarbamoylcinchonidine (anti-open conformation) with (*all*-*S*)-DNB-Ala$_2$ in a tentative model of the complex.

Taking into account all results described above, the chiral discrimination between the (*all*-*R*)- and (*all*-*S*)-enantiomers of **SA1** and **SA2** is reflected in the conformational status of the chiral selector. Moreover, the fact that the conformations of all four complexes deviate from that of **SO1·HCl** shows that the conformational changes upon complexation are not solely related to the protonation of **SO1** but must also include additional molecular interaction increments, which obviously differ in magnitude and/or direction (attraction or repulsion) for the enantiomers. However, the conformational differences between the (*all*-*R*)- and the (*all*-*S*)-complexes were similar for both the di- and the tripeptide. This similarity

TABLE 2. ^{1}H NMR Chemical Shifts (δ) of Selector, Selectands, and Selector−Selectand Complexes and Complexation-Induced Shifts ($\Delta\delta$)

	δ (ppm)[a]						$\Delta\delta$ (ppm)[b]			
proton[c]	free forms[d]	ionized forms[e]	(*S*,*S*)-complex	(*R*,*R*)-complex	(*S*,*S*,*S*)-complex	(*R*,*R*,*R*)-complex	(*S*,*S*)-complex	(*R*,*R*)-complex	(*S*,*S*,*S*)-complex	(*R*,*R*,*R*)-complex
H2′	8.65	8.78	8.60	8.68	8.66	8.68	−0.05	0.04	0.02	0.04
H3′	7.54	7.71	7.50	7.57	7.56	7.57	−0.04	0.04	0.02	0.04
H5′	7.50	7.59	7.14	7.48	7.38	7.49	−0.36	−0.02	−0.12	−0.01
H7′	7.46	7.63	7.20	7.51	7.44	7.51	−0.26	0.05	−0.03	0.05
H8′	7.96	8.07	7.75	7.99	7.93	8.00	−0.22	0.03	−0.03	0.03
H2a	2.65	3.35	3.14	3.04	3.10	3.07	0.49	0.39	0.45	0.42
H2b	3.08	3.65	3.75	3.40	3.47	3.42	0.67	0.32	0.39	0.35
H3	2.35	2.86	2.73	2.63	2.68	2.66	0.38	0.28	0.32	0.30
H4	1.83	2.18	2.05	2.02	2.04	2.04	0.22	0.19	0.21	0.21
H5a	1.61	2.03	1.93	1.84	1.88	1.86	0.33	0.23	0.27	0.26
H5b	1.91	2.32	2.21	2.11	2.16	2.13	0.30	0.20	0.25	0.22
H6a	2.72	3.39	3.35	3.08	3.12	3.11	0.64	0.36	0.40	0.39
H6b	3.26	3.73	3.44	3.50	3.51	3.52	0.18	0.25	0.25	0.27
H7a	1.69	1.86	1.65	1.78	1.75	1.79	−0.03	0.09	0.06	0.10
H7b	1.83	2.30	2.12	2.06	2.10	2.09	0.29	0.23	0.26	0.25
H8	3.24	3.84	3.65	3.57	3.63	3.62	0.41	0.33	0.39	0.38
H9	6.47	6.87	7.12	6.63	6.80	6.65	0.65	0.16	0.33	0.17
H10	5.81	5.82	5.75	5.82	5.80	5.82	−0.07	0.01	−0.01	0.01
H11a	4.95	5.09	5.00	5.03	5.03	5.03	0.05	0.08	0.08	0.09
H11b	5.00	5.17	5.09	5.09	5.10	5.10	0.09	0.09	0.10	0.10
H12a[f]	3.87	3.93	3.59	3.87	3.79	3.87	−0.27	0.00	−0.08	0.00
H12b[f]	3.87	4.02	3.68	3.90	3.84	3.91	−0.19	0.03	−0.03	0.04
H14	1.12	1.14	1.13	1.13	1.13	1.13	0.01	0.01	0.01	0.01
H16	n.d.[g]	n.d.[g]	n.d.[g]	n.d.[g]	n.d.[g]	n.d.[g]	n.d.[g]	n.d.[g]	n.d.[g]	n.d.[g]
H18	1.27	1.29	1.41	1.28	1.31	1.28	0.13	0.01	0.04	0.01
H202	4.43	4.22	4.22	4.33			−0.21	−0.10		
H203	1.44	1.38	1.44	1.42			0.00	−0.02		
H204	n.d.[g]	n.d.[g]	n.d.[g]	n.d.[g]			n.d.[g]	n.d.[g]		
H206	4.63	4.63	4.78	4.63			0.14	−0.01		
H207	1.53	1.53	1.59	1.53			0.06	0.00		
H208	n.d.[g]	n.d.[g]	n.d.[g]	n.d.[g]			n.d.[g]	n.d.[g]		
H211+ H215	9.10	9.13	8.80	9.11			−0.30	0.00		
H213	9.13	9.13	8.62	9.12			−0.51	−0.01		
H302	4.37	4.15			4.28	4.28			−0.10	−0.09
H303	1.41	1.36			1.39	1.39			−0.02	−0.02
H304	n.d.[g]	n.d.[g]			n.d.[g]	n.d.[g]			n.d.[g]	n.d.[g]
H306	4.42	4.39			4.41	4.41			−0.01	−0.01
H307	1.41	1.41			1.40	1.41			−0.01	0.00
H308	n.d.[g]	n.d.[g]			n.d.[g]	n.d.[g]			n.d.[g]	n.d.[g]
H310	4.60	4.63			4.63	4.61			0.03	0.01
H311	1.53	1.57			1.54	1.55			0.01	0.02
H312	n.d.[g]	n.d.[g]			n.d.[g]	n.d.[g]			n.d.[g]	n.d.[g]
H315 + H319	9.11	9.12			9.05	9.10			−0.06	−0.01
H317	9.14	9.13			9.05	9.12			−0.09	−0.01

[a] All ppm values are referenced to residual methanol (δ = 3.31 ppm). [b] Complexation-induced shifts (reported relative to the free forms); negative values denote upfield shifts. [c] For numbering of protons see Figure 3. [d] **SO1**/**SA1**, **SA2**. [e] **SO1·HCl**/sodium salts of **SA1**, **SA2**. [f] Arbitrary assignment of the shifts to the two protons. [g] Not detected.

is remarkable, since the levels of enantiodiscrimination are considerably different for these two analytes.

2.5. Complexation-Induced Shifts upon Enantioselective Binding. Chemical shift changes occurring upon complexation of the chiral selector and a selectand enantiomer were studied to gain information on the intermolecular interactions responsible for enantiomer discrimination as well as on the relative orientation of the association partners in the complexes. Because the primary interaction involved in complexation is a (non-enantioselective) ion-pair formation, the protonation and deprotonation of the chiral selector and the selectand, respectively, are expected to induce strong complexation-induced shifts (CISs).

To deconvolute the effects of ionization from the other intermolecular interactions present in the complexes, the changes induced by the protonation of **SO1** and the deprotonation of **SA1** and **SA2** were investigated by comparing the chemical shifts observed for the free base **SO1** and **SO1·HCl** as well as for the free acids **SA1** and **SA2** and their sodium salts (Table 2). Protonation of **SO1** deshielded all protons, leading to pronounced downfield shifts of the protons of the quinuclidine moiety and of H_9 (generally in the range of 0.4−0.7 ppm), while the shifts of the quinoline protons were considerably smaller ($\delta \approx 0.1-0.2$ ppm). These observations confirm that the quinuclidine nitrogen is the sole site of protonation (compare section 2.3). All other protons experienced only small chemical shifts, with those of the *tert*-butyl groups being practically unaffected. Deprotonation of **SA1** and **SA2** had a significant impact only on the protons attached to the C-terminal chiral center (H_{202}/H_{302}), which shifted upfield by ≈0.2 ppm.

By using this information, the chemical shifts of the protons in the complexes were evaluated with respect to significant CISs. For the complexes of the **SA1** enanti-

omers these CISs are depicted in Figure 4a alongside the respective ionization-induced CISs. The complex of **SO1** with (*all-S*)-**SA1** showed extensive downfield shifts of the quinuclidine protons, indicating extensive protonation. However, protons H_{2a}, H_{6b}, H_{7a}, and H_{7b} exhibited considerably smaller shifts relative to the free form of **SO1** than were found for **SO1·HCl** ($\Delta > 0.2$ ppm, Table 2). This can be explained by **SA1** being a weaker acid than HCl and the different geometry of the **SA1** anion compared to chloride. Very pronounced upfield shifts were noted for the quinoline's $H_{5'}$, $H_{7'}$, and $H_{8'}$ protons. The same behavior was observed for the $H_{12a,b}$ protons located in close proximity to $H_{5'}$ and $H_{7'}$. An analogous trend was found for the aromatic protons of (*all-S*)-**SA1**, with H_{213} being shifted upfield 0.51 ppm. These findings provide striking evidence for strong $\pi-\pi$-interactions between the aromatic groups of **SO1** and (*all-S*)-**SA1**, which effect mutual shielding. Another strong CIS occurred for the H_9 signal. The downfield shift (0.65 ppm) can only partly be explained by the deshielding effect of **SO1** protonation (see Figure 4a). The additional shift may be explained by the change of conformation upon complexation (see above) moving H_9 into deshielding regions of the quinoline moiety or the carbamate carbonyl group. Finally, an interesting downfield shift of the H_{18} protons of the *tert*-butyl carbamate was noted. As the carbamoyl group of a related chiral selector was found to form a hydrogen bond with the C-terminal amide of (*all-S*)-**SA1**,[5] it seems very likely that the carbamoyl group of **SO1** engages in hydrogen bonding with (*all-S*)-**SA1**, which then causes the deshielding of the H_{18} protons. Contrary to these findings, no specific CISs were found for the complex of **SO1** with (*all-R*)-**SA1**. The upfield shifts of the quinuclidine protons result from the ion-pair formation that constitutes the primary interaction force for this complex as well. For most protons these shifts are somewhat smaller than those observed for the complex of **SO1** with (*all-S*)-**SA1**, which may reflect a lower proportion of the selectand being present in the complexed form. This relates to a smaller complexation constant for this enantiomer, which as a consequence leads to lower chromatographic retention (see above). The less pronounced upfield shift of H_9 compared to the (*all-S*)-**SA1** complex (0.16 ppm versus 0.65 ppm) results from the different conformation (see above). The signals of the aromatic protons of both selector and analyte remained almost unaffected by the complexation process, indicating the absence of $\pi-\pi$-interactions, which thus seem to play an important role for enantiomer discrimination.

The results obtained for the complexes of **SO1** with the **SA2** enantiomers (see Figure 4b and Table 2) showed a very different picture. The upfield shifts of the quinuclidine protons were practically identical for both complexes, indicating a very similar degree of protonation. Their extent was considerably smaller than that of the shifts noted for the complex of **SO1** with (*all-S*)-**SA1**. This finding seems to point toward small complexation constants for both **SA2** enantiomers, their similar magnitude resulting in only modest enantioselectivity. This deduction is supported by the HPLC results, where small retention factors were found for both enantiomers of **SA2**. The comparison of the CISs observed for the aromatic protons of both **SO1** and the (*all-R*)- and (*all-S*)-enantiomers of **SA2** for the two diastereomeric complexes showed that some differences still exist (see Figure 4b); however, their magnitude is much smaller than for the complexes of **SA1**. Thus, the stereoselective $\pi-\pi$-interactions, which are a major contributor to enantioselectivity, are largely lost upon elongation of the peptide chain from the dipeptide (**SA1**) to the tripeptide (**SA2**). Most probably, steric constraints do not allow ion-pairing and $\pi-\pi$-stacking to take place simultaneously. The resonances of the H_{18} protons are almost unchanged relative to the free selector, suggesting the absence of hydrogen bonding for the complexes of both **SA2** enantiomers. Overall, the differences between the diastereomeric complexes of the two enantiomers of **SA2** are much smaller than those between the complexes of the **SA1** enantiomers, which is also reflected by the smaller CIS differences of H_9 (0.16 ppm versus 0.49 ppm).

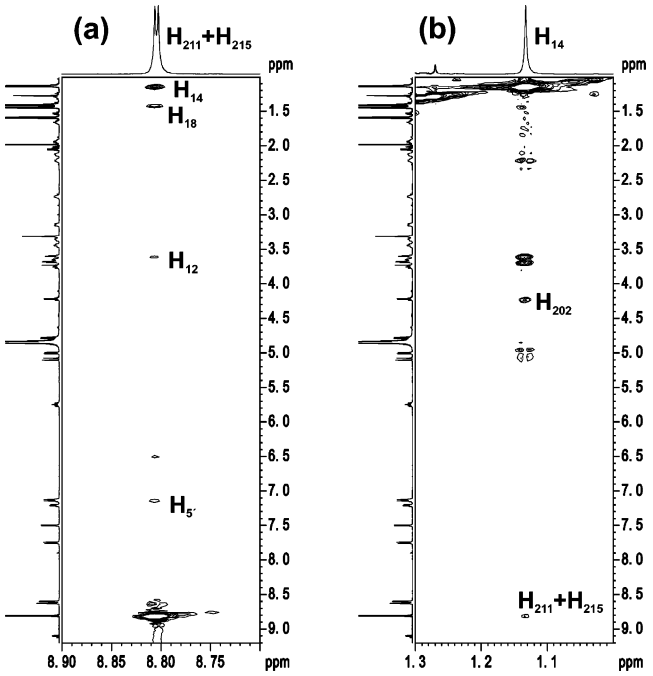

FIGURE 6. NOESY spectra of the 1:1 complex of 6′-neopentoxy-9-*O*-*tert*-butylcarbamoylcinchonidine with the (*all-S*)-enantiomer of DNB-Ala_2 showing intermolecular interactions of (a) the analyte's DNB group (ortho protons H_{211} and H_{215}) and (b) the selector's neopentyl group (*tert*-butyl protons H_{14}).

2.6. Spatial Arrangement of Selector and Selectands in Solution. To further elucidate the geometry of the complexes, i.e., the relative arrangement of the chiral selector and the analyte enantiomer, the NOESY spectra (available as Supporting Information) were scanned for the presence of resonances evoked by close intermolecular contacts.[22,23] For the complex of **SO1** and (*all-S*)-**SA1** several intermolecular NOEs were detected (Figures 5 and 6). One was found between an aromatic ortho-proton of **SA1** ($H_{211/215}$) and $H_{5'}$, further supporting the proposed presence of face-to-face $\pi-\pi$-stacking. The $H_{211/215}$ protons of the 3,5-dinitrobenzoyl group also showed intermolecular NOEs with the protons of the selector's neopentyl group ($H_{12a,b}$ and H_{14}), suggesting a

(22) Pirkle, W. H.; Pochapsky, T. C. *J. Am. Chem. Soc.* **1986**, *108*, 5627−5628.
(23) Pirkle, W. H.; Pochapsky, T. C. *J. Am. Chem. Soc.* **1987**, *109*, 5975−5982.

TABLE 3. Averaged Potential Energies, Component Energies, and Solvation Energies (kJ·mol^{-1}) for the Interactions of the Complexes of SO1 with SA1 and SA2

	SO1 + (*all-R*)-**SA1**	**SO1** + (*all-S*)-**SA1**	ΔE^a	**SO1** + (*all-R*)-**SA2**	**SO1** + (*all-S*)-**SA2**	ΔE^a
total energy	−651.3	−658.1	−6.8	−730.5	−734.5	−4.0
stretch	156.9	155.0	−1.9	169.3	170.7	1.4
bend	205.7	206.6	0.9	224.2	222.5	−1.7
torsion	120.0	118.4	−1.6	128.6	126.9	−1.7
van der Waals	28.7	26.3	−2.4	36.3	32.3	−4.1
electrostatic	−939.6	−956.4	−16.8	−1044.5	−1048.2	−3.7
solvation	−223.0	−208.0	15.0	−244.3	−238.5	6.2

[a] A negative value means that the (*all-S*)-complex is more stable.

well-defined arrangement of the quinoline ring plus its 6′-residue and the N-terminus of the 3,5-dinitrobenzoylated peptide, as well as with the protons of the *tert*-butylcarbamoyl group (H_{18}). The observation of NOE signals between the $H_{211/215}$ protons and several protons of **SO1**, which are located in different regions of the selector molecule, may be explained by the simultaneous presence of two or more different relative arrangements of the selector and the analyte within the complex. Finally, an intermolecular NOE was noted between the *tert*-butyl protons of the neopentyl group of **SO1** (H_{14}) and the proton attached to the chiral center of the C-terminal amino acid of SA1 (H_{202}). On the contrary, no intermolecular NOEs were found in the spectrum of the complex of **SO1** with (*all-R*)-**SA1**. This observation is consistent with the weaker binding of the (*all-R*)-enantiomer seen in the HPLC and CIS studies as well as with the absence of $\pi-\pi$-stacking. For the **SA2** complexes no intermolecular NOEs were observed for both enantiomers, which is consonant with the considerably weaker intermolecular interactions noted for these two complexes above and the almost complete loss of $\pi-\pi$-stacking also for the more strongly bound (*all-S*)-enantiomer.

2.7. Energetics of Complexation with SO1. Computational chemistry allows one to extract information about intermolecular interactions not amenable to experimentation. However, before one can assess these structural details, it must be ensured that essential experimental findings, such as the HPLC elution order, the differential free energies of the competing diastereomeric complexes, and the intra- and intermolecular NOEs, are reproduced by the computations.

Anticipating that $\pi-\pi$-interactions may be involved in the intermolecular association of the selector with the selectands, the computations were performed with use of a force field approach. This method is preferable over density functional theory (DFT) for the following reasons: With the latter method only picosecond simulation times are possible compared to nanosecond results obtainable with a force field. Second, as described in a recent paper,[24] DFT treats $\pi-\pi$-stacking poorly. For example, DFT methods fail completely to describe the attraction in the benzene dimer.[24]

To account for the polar chromatographic conditions used to evaluate the differential free binding energies we implemented a polar solvent model in our simulations. This solvent model is a continuum model of water and it is expected that a pure water model may not reproduce exactly the experimental condition of a mixed hydro-organic solvent. Total energies and solvation energies for these simulations are presented in Table 3. Because the total interaction energies consist of energies from bond stretching, angular deformation, and other contributing force field terms, the time-averaged component energies for all four complexes are also presented in Table 3. The differences in energies between the (*all-R*)- and (*all-S*)-complexes are given by ΔE, where a negative value means the (*all-S*)-complex is more stable.

The results from these nanosecond simulations indicate that the more retained enantiomer, corresponding to the more stable complex, has (*all-S*)-configuration for both **SA1** and **SA2**. This is consonant with experiment. The computed energy difference for the **SA1** complexes (−6.8 kJ·mol^{-1}) underestimates slightly the experimental value (−7.4 kJ·mol^{-1}) while for the **SA2** complexes the energy difference (experimental = −2.6 kJ·mol^{-1}, computed = −4.0 kJ·mol^{-1}) is overestimated. Hence, from these simulations we find that the computed retention order is correct for both selectands, while the differential free energies of binding are reproduced well by the AMBER* force field with use of a water continuum model for **SA1** but less well for **SA2**.

We now consider the component energy terms in Table 3. For **SA1**, less stretching deformation is observed for the more stable (*all-S*)-complex than for the (*all-R*)-complex ($\Delta E \approx 2$ kJ·mol^{-1}). For **SA2** this difference is ≈1 kJ·mol^{-1} and it favors the (*all-R*)-complex. The bending deformation energies for the **SA1** complexes are similar in magnitude and favor the (*all-R*)-enantiomer, while they are larger for the **SA2** complexes and favor the (*all-S*)-enantiomer. The torsional deformation energies are similar for the complexes of both enantiomers of **SA1** as well as **SA2**. For both selectands the more stable complex contains less torsional deformations than the less stable one. Even though these differences are small in magnitude, it is evident that there are clear differences in the energetics of the **SA1** enantiomers which are very well discriminated by **SO1** versus the **SA2** enantiomers which are relatively poorly discriminated.

The above-mentioned component energies are all considered to arise from "bonding" terms in the force field because atoms involved in those terms are connected to one another contiguously. Contrarily, the remaining three component energies in Table 3 involve "nonbonded" interactions, i.e., atom−atom interactions that are 1,3 or greater in nature. In the **SA1** simulations the van der Waals (vdW) terms are within 2.4 kJ·mol^{-1} of one another. For **SA2** the energy difference is larger (4.1 kJ·mol^{-1}). In both instances, however, there is less vdW

(24) Czernek, J. *J. Phys. Chem. A* **2003**, *107*, 3952−3959.

TABLE 4. Intermolecular Energies (kJ·mol^{-1}) of the Complexes of SO1 with SA1 and SA2

	SO1 + (*all-R*)-**SA1**	**SO1** + (*all-S*)-**SA1**	ΔE^a	**SO1** + (*all-R*)-**SA2**	**SO1** + (*all-S*)-**SA2**	ΔE^a
total energy	−505.7	−529.5	−23.8	−480.0	−497.9	−17.8
van der Waals	−22.8	−23.1	−0.3	−6.1	−14.3	−8.2
electrostatic	−482.9	−506.4	−23.5	−473.9	−483.0	−9.1

[a] A negative value means that the (*all-S*)-complex is more stable.

energy associated with the (*all-S*)-complexes, indicating that there exists a better selector-analyte fit for the (*all-S*)-complexes than for the (*all-R*)-complexes. The electrostatic energies heavily favor the more stable (*all-S*)-complex by 16.8 kJ·mol^{-1} for **SA1**. The genesis of this stabilization is that the (*all-S*)-complex fits together better than the (*all-R*)-complex. Because the electrostatic attractions fall off with the square of the distance between charges, even very small structural changes can give rise to large stabilization energies. We point out here that the energies described above refer to all atom−atom interactions in the complex, i.e., the energies in Table 3 are a composite of both intramolecular and intermolecular energies. Below we will extract from these data only the intermolecular energies and discuss them separately with respect to chiral discrimination. For **SA2**, in contrast, we find that the electrostatics and the vdW energy differences are comparable in magnitude and favor the (*all-S*)-complex but to a lesser extent than for **SA1**.

2.8. Intermolecular Forces Leading to Chiral Discrimination. To obtain a more detailed picture of the enantiodiscriminating process, the intermolecular forces responsible for chiral discrimination need to be extracted from the simulation data. The intermolecular terms that need to be considered are only the nonbonded vdW energy and the electrostatic energies, hereafter simply called "nonbonded" energies. It is important to recognize that the nonbonded energies in Table 3 are composites of intramolecular and intermolecular energies. In molecular mechanics force fields the nonbonded interactions are computed pairwise additive meaning that all atoms experience all other nonbonded atoms regardless of whether those other atoms are part of the same molecule or of a different one. We have written a program that extracts from these data only the intermolecular components.[25] Those values, averaged over the simulation time period, are presented in Table 4.

Several points of significance are derived from Table 4. First, both the van der Waals and the electrostatic interactions between the molecules are attractive (negative energies). Second, the dominant stabilizing force holding each complex together is from the electrostatic term. In this regard we see that for the **SA1** complexes 95% of the total intermolecular energy is attributable to electrostatic attractions, while 97−99% is due to electrostatics for the **SA2** complexes. Third, the most insightful aspect of these results concerning chiral recognition is the *difference* in energy between the diastereomeric complexes, denoted as ΔE in Table 4. This difference is a measure of chiral discrimination.

While we find both the vdW and electrostatic attractions between the molecules in the binary complexes favoring the (*all-S*)-enantiomers, the larger enantiodiscriminating force is attributed to the long-range electrostatic effects rather than to the short-range dispersion forces. We point out that this discriminating force does not arise exclusively from the ion-pair formed between the carboxylates of the selectands and the quinuclidine nitrogen of the selector. Even though those regions of the molecule are formally charged, all other atoms have partial atomic charges and they too are contributing to the electrostatic discriminating energies. In a forthcoming section we will focus on which fragments of the selector are actually most responsible for chiral discrimination. At this point we again highlight the difference between the complexes of the well-separated **SA1** and the poorly resolved **SA2** enantiomers. In the former system the intermolecular chiral discrimination is almost exclusively effected by electrostatic forces, while in the latter the vdW and electrostatic forces are contributing almost equally.

The intermolecular energies listed in Table 4 are average values; they do not indicate how those energies can fluctuate in time nor do they describe the distribution of energies that occurred during the simulation time period. During the simulation, as the molecules are free to move about and collide with one another, both the inter- and intramolecular forces have changed. There are two ways of visualizing these changes, the first being plots of how the intermolecular energies between **SO1** and the analyte enantiomers change as a function of time (trajectories). Huge variations in intermolecular energy were observed as the system evolves in time with a similar behavior for all four complexes. These trajectories are available as Supporting Information. In particular, due to thermal collisions the selectand moves and reorients itself with respect to the selector, albeit while remaining in a localized binding region around **SO1**. During this reorientation both the electrostatic and vdW energies are undergoing large fluctuations in magnitude (the sharp, noise-like spikes in the figures).

Another way of visualizing the intermolecular forces is to make plots of the distribution of energies that were observed during the total simulation time period. In these figures the energies, binned in units of 2 kJ·mol^{-1}, are plotted as a function of the number of times a particular energy was encountered during the simulation time period. As the figures for the complexes of **SA1** and **SA2** showed similar patterns, only the plots for **SA1** are presented here (Figure 7), those for **SA2** being available as Supporting Information. In the plots of the vdW energies (Figure 7e,f) note that some values are negative (net attraction) while others are positive (net destabilization). In contrast, the electrostatic energies (Figure 7c,d) are always negative and attractive.

The distribution of electrostatic interactions between selector and selectand is unimodal with a quasi-normal

(25) Peterson, M. A. Understanding Enantiodifferentiation Through Molecular Simulations, Ph.D. Thesis, Purdue University, 1996.

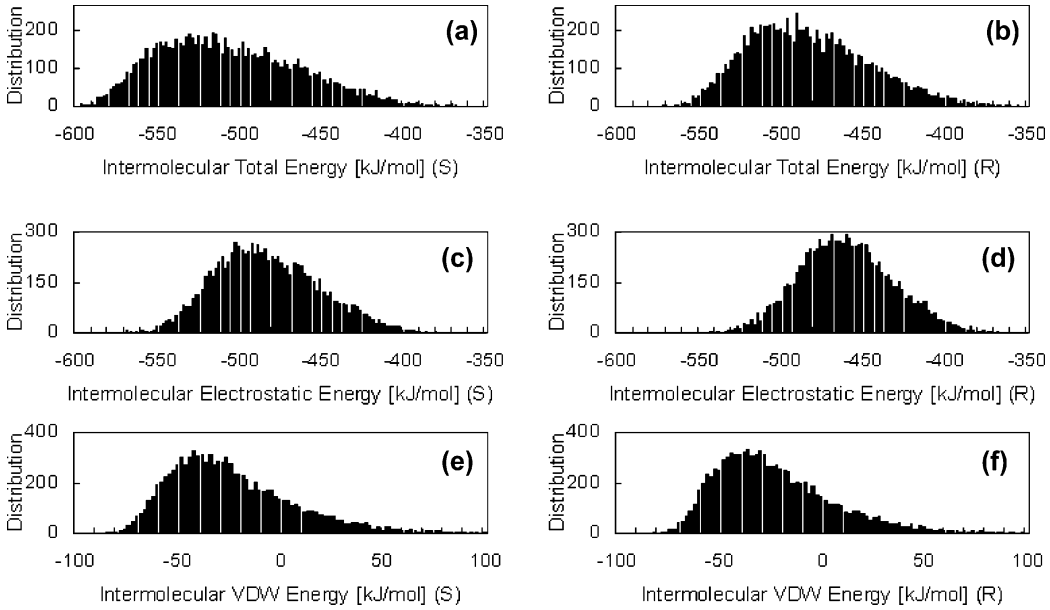

FIGURE 7. Distributions of the total intermolecular energy (a, b), the intermolecular electrostatic energy (c, d), and the intermolecular van der Waals energy (e, f) for the (*all-S*)-enantiomer (a, c, e) and the (*all-R*)-enantiomer (b, d, f) of **SA1** interacting with **SO1**.

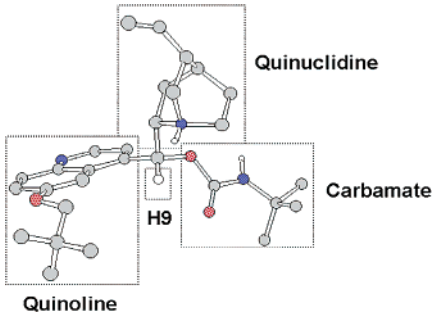

FIGURE 8. Partitioning of **SO1** into four molecular fragments.

(Gaussian) distribution for all complexes. The centers of the distributions of the more tightly bound (*all-S*)-enantiomers are shifted to more negative (attractive) energies than for the corresponding (*all-R*)-antipodes as expected. The plots further illustrate that the shapes of the distributions for the (*all-R*)- and the (*all-S*)-enantiomers interacting with **SO1** are not much different from one another, indicating that only very subtle differences in intermolecular interactions are involved in the discrimination process.

2.9. Fragment Interactions. To better understand how **SO1** binds and discriminates between the analyte enantiomers we consider now the interactions of molecular fragments that constitute the chiral selector. We emphasize here that fragment energies are accessible by computations only and not by experiment. Partitioning the selector into fragments is a subjective and arbitrary decision. However, because there exist several characteristic, identifiable groups comprising this SO we have divided the molecule into the four segments that are linked to C_9 as illustrated in Figure 8.

In Table 5 we compile the average intermolecular energies associated with each of these fragments interacting with the analyte molecule as well as the van der Waals and electrostatic contributions. Note that the sums of energies in Table 5 are slightly smaller than that in Table 4 because C_9 was not included in the calculation of the fragment energies.

From this analysis we find that the fragment most responsible for holding the complexes together is the quinuclidine group (see Table 5). The second most stabilizing interaction comes from the quinoline ring. This ring is seen in molecular graphics movies to form $\pi-\pi$-stacking associations with the 3,5-dinitrobenzoyl group of the analyte (see below). The carbamate fragment, being positive in energy, is actually repulsive. This is a consequence of the molecules being held together tightly by electrostatic forces and some parts of the complexes are experiencing steric repulsions due to congestion.

The second major point concerning these results involves the difference each fragment experiences when associating with each selectand enantiomer. This difference is a measure of chiral discrimination. For the **SA1** complexes the fragment showing the greatest difference between the enantiomers is the carbamate moiety. In contrast, the enantiodiscrimination arising from the carbamate when **SA2** binds to **SO1** is negligible; in this system the most enantiodiscrimination is associated with the quinoline moiety. In an earlier paper where simulations were carried out for **SO1** and a 3,5-dinitrobenzoyl leucine analyte we found that the most discriminating fragment was the carbamate.[12] In that study the chromatographic enantioselectivity was extremely large ($\alpha =$ 32.6) as for the **SA1** system described here. Hence, a pattern is emerging from the simulation results: effective chiral recognition by the cinchona alkaloid carbamate receptors involves large enantiodiscrimination by the carbamate moiety. It is clear here that the **SA2** enantiomers, which are resolved with considerably less selectivity, do not experience this type of discrimination. This is in accordance with the CISs results (see above). Finally,

TABLE 5. Intermolecular Energies (kJ·mol^{-1}) for Fragments of the Complexes of SO1 with SA1 and SA2

fragment	intermolecular energy	**SO1** + (*all-R*)-**SA1**	**SO1** + (*all-S*)-**SA1**	ΔE^a	**SO1** + (*all-R*)-**SA2**	**SO1** + (*all-S*)-**SA2**	ΔE^a
quinoline	total	−84.6	−100.5	−15.9	−75.8	−92.1	−16.3
	van der Waals	−45.5	−47.0	−1.5	−33.6	−35.2	−1.6
	electrostatic	−39.2	−53.5	−14.3	−42.2	−56.9	−14.7
quinuclidine	total	−410.4	−400.2	10.2	−416.7	−414.9	1.8
	van der Waals	38.5	39.4	0.9	39.9	38.8	−1.1
	electrostatic	−448.8	−439.6	9.2	−456.5	−453.6	2.9
carbamate	total	68.3	48.0	−20.3	67.7	67.0	−0.7
	van der Waals	−14.3	−14.2	0.1	−10.8	−16.0	−5.2
	electrostatic	82.6	62.2	−20.4	78.5	83.0	4.5
hydrogen H_9	total	−15.6	−14.6	1.0	−15.6	−16.2	−0.6
	van der Waals	0.5	0.9	0.4	0.2	0.2	0.0
	electrostatic	−16.2	−15.5	0.7	−15.6	−16.2	−0.6

[a] A negative value means that the (*all-S*)-complex is more stable.

we see from Table 5 that for fragments that are most discriminating, the differential interaction energy (ΔE) is larger for electrostatic contributions than for vdW contributions. Hence, these fragments discriminate primarily by long-range electrical effects rather than by short-range dispersion forces.

Another way to discuss these fragmentation energies is to plot the distribution of intermolecular energies for each fragment. For each fragment the electrostatic energies, the vdW energies, and the total intermolecular energies of all four complexes are available as Supporting Information. Regardless of which enantiomer binds to **SO1** we find that most of the plots are similar in shape, varying only slightly in their skewness. In some instances, however, there are distinct differences, e.g. for the electrostatic energy distributions of the quinoline fragment for the complex of **SO1** with **SA1**, where the distribution for the (*all-S*)-enantiomer has bimodal character while that for the (*all-R*)-enantiomer is unimodal. The shapes of these distributions may serve as key signatures associated with chiral recognition, a topic that we are pursuing.

2.10. Structural Features—Comparisons with NMR Data. One experimental key finding is that an intermolecular NOE exists between an aromatic ortho-proton ($H_{211/215}$) of (*all-S*)-**SA1** and $H_{5'}$ of **SO1** in the complex. The propinquity of the π-acidic and π-basic aromatic rings (visualized from MD trajectories as $\pi-\pi$-stacking) extracted from the molecular simulation data is consistent with this finding. An illustration of the $\pi-\pi$-stacking distance is shown in Figure 9. It is to be noted in this figure that both enantiomers form $\pi-\pi$-stacking but the more stable (*all-S*)-enantiomer can form better $\pi-\pi$-stacking, which shows up as a greater number of short-range distances in the histogram.

The $H_{211/215}$ protons also sense the hydrogens of the selector's neopentyl group. The average distance between the $H_{211/215}$ protons and the terminal methyl protons of the neopentyl group (H_{14}) was computed to be 5.85 Å. This distance is larger than one anticipates for two reasons. First, we are using a pure water solvent to carry out the simulations compared to a methanol solution used experimentally. The more polar aqueous phase is oversolvating the ionic complex making it less tight than it would be in a less polar solvent. Second, and more important, we are reporting an average value here. This average includes many configurations where part of the system has dissociated and then reassociated during the simulation. What is important is that there exist many short-range interactions which relate to the NOE (in addition to the non-NOE-inducing long-range contacts). A relevant paper describing short-range and long-range proton—proton distances obtained from MD simulations and their relationship to NOE observations has been published by Feller et al.[26]

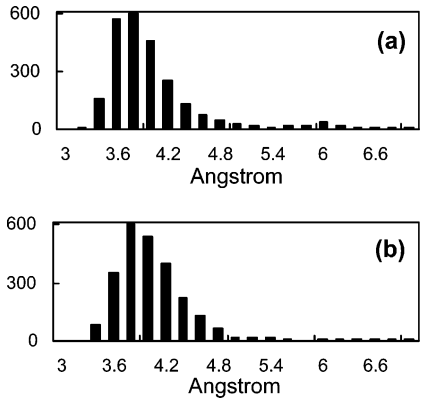

FIGURE 9. Distribution of intermolecular distances between the aromatic ring centroids of **SO1** and the (*all-S*)-enantiomer (a) and the (*all-R*)-enantiomer (b) of **SA1**. The distance between the centroids is related to $\pi-\pi$-stacking in the complexes.

Another NOE of the aromatic ortho-protons also indicates the proximity of the carbamate's *tert*-butyl group. The computed average distance between these hydrogens is 4.87 Å, a value that is again somewhat overestimated for the same reasons as above. Finally, the proton attached to the stereogenic center of the C-terminal amino acid of **SA1** (H_{202}) shows an interaction with the *tert*-butyl protons of the neopentyl group of **SO1**. The computed average distance between these protons is 5.03 Å. Hence, most intermolecular NOEs found experimentally could be computationally reproduced in terms of appropriate distances between the respective protons.

3. Conclusions

An advanced understanding of the chiral recognition mechanism governing the enantioselective binding of *N*-3,5-dinitrobenzoyl derivatives of dialanine and triala-

(26) Feller, S. E.; Huster, D.; Gawrisch, K. *J. Am. Chem. Soc.* **1999**, *121*, 8963−8964.

nine peptides ("selectands" **SA1** and **SA2**, respectively) and 6′-neopentoxy-9-*O*-*tert*-butylcarbamoylcinchonidine (**SO1**) has been achieved employing a combination of chromatographic and NMR spectrocopic experiments as well as molecular modeling.

Liquid chromatographic experiments performed with a chiral stationary phase comprising an immobilized version of **SO1** showed that the (*all-S*)-enantiomers of **SA1** and **SA2** were bound more strongly than the corresponding (*all-R*)-enantiomers, indicating closely related enantioselective binding mechanisms. The level of enantioselectivity, however, was found to depend on the number of interlinked amino acids. While a very high enantioselectivity factor of $\alpha = 20.0$ was observed for **SA1**, the enantiomers of **SA2** were significantly less well separated ($\alpha = 2.8$). Thus, in terms of differential free energy, the insertion of an additional amino acid into the dipeptide backbone induced a dramatic loss of 4.9 $kJ \cdot mol^{-1}$. This observation suggested an unfavorable change of stereoselective binding increments. Thus, the relative contributions of the intermolecular interaction increments being responsible for this phenomenon were assessed by an in-depth NMR study of the four complexes between **SO1** and the (*all-R*)- and (*all-S*)-enantiomers of **SA1** and **SA2**, respectively.

Continuous variation-type titration experiments established 1:1 stoichiometry for all complexes, indicating that only the (more basic) quinuclidine nitrogen of **SO1** is involved in the binding of the acidic analytes. The analysis of inter-ring NOEs between the quinoline and quinuclidine protons of **SO1** provided evidence for the existence of three specific conformations of the selector, the relative populations of which depended on its protonation status and the nature and stereochemistry of analyte associated with **SO1**.

While a mixture of open and closed conformers was detected for the free **SO1**, only the anti-open conformation was observed for the selector upon protonation or complexation with the more strongly bound (*all-S*)-enantiomers of both selectands. Contrarily, all three conformations were found for the complexes of the (*all-R*)-enantiomers, although a higher proportion of the anti-open state than for the free **SO1** was noted. The conformational differences between the (*all-R*)- and the (*all-S*)-complexes were similar for both the di- and the tripeptide.

Complexation-induced shifts (CISs) were studied to acquire information on the nature and strength of the intermolecular interactions active in the complexes. Thereby, the large effects of unspecific ionization of the binding partners were taken into account separately to allow an unhindered assessment of the effects of the enantioselective interactions. The chemical shifts observed for the two (*all-R*)-complexes of **SA1** and **SA2**, respectively, were practically identical in all cases and no specific CISs were observed. The two (*all-S*)-complexes showed several CISs in the same directions but their extent was much smaller for the **SA2** complex, indicating a loss of hydrogen bonding and a strong reduction of $\pi-\pi$-interactions.

Finally, the relative arrangements of the selector and the selectands were investigated based on the observed intermolecular NOEs. The NOESY spectrum of the complex of **SO1** with (*all-S*)-**SA1** showed several resonances with intermolecular NOEs involving the aromatic ortho-protons of the 3,5-dinitrobenzoyl group of **SA1**, once again indicating the presence of $\pi-\pi$-stacking. No intermolecular NOEs were observed for the two complexes of the (*all-R*)-configured analytes nor for the complex of (*all-S*)-**SA2**, which is in agreement with a less tight binding of the selectands to the selector in these complexes.

Besides the NMR investigations, nanosecond stochastic dynamics simulations on the complexes were carried out by using a polar continuum model for solvent. The simulation results agree with all experimental facts including the following: (1) The retention orders were correctly computed with the (*all-S*)-enantiomers being longer retained on the column. (2) The computed energy difference for the well-separated **SA1** was reproduced very well, while that for **SA2** is slightly overestimated. (3) Most intermolecular NOEs depicted in Figure 5 are accounted for by close contacts between the respective atom pairs during the simulation. On the basis of the good agreement between experiment and theory, information extracted from the simulations was deemed reliable.

Force field component energies for the complexes were analyzed and differences between the complexes were explained. More important, however, was the extraction of the intermolecular energies giving rise to complex formation as well as to stereodiscrimination. In all instances the intermolecular force most responsible for formation of the complexes is electrostatic in nature. For **SA1**, which is highly discriminated by **SO1**, we find that chiral recognition is almost exclusively electrostatic, while the poorly resolved **SA2** has an equal mixture of van der Waals and electrostatic forces contributing to the discrimination.

To visualize the numerical data derived from the simulations different forms of presentation were provided for the purpose of better illuminating the differences between the various complexes as well as to illustrate their similarities. Histogram plots of energy distributions were provided in addition to typical MD trajectories. Plots of intermolecular van der Waals energies, intermolecular electrostatic energies, and their sums (total intermolecular energies) revealed similar unimodal energy distributions with the center of those distributions shifted to lower energies for the more stable complexes. The widths and shapes of the distributions, albeit different for the (*all-S*)- versus the (*all-R*)-complexes, are surprisingly similar, thus highlighting the fact that the intermolecular forces giving rise to chiral discrimination differ only in very subtle ways.

It was assessed which fragments of the chiral selector are most responsible for analyte binding as well as for enantiomer discrimination. The roles of these fragments differ for the two peptide analytes (**SA1** versus **SA2**). Intermolecular energies were presented as histogram distribution plots to illustrate the similarities and differences between the fragment energies of the various complexes. It was found that effective chiral recognition by the cinchona carbamate receptors involves large stereoselective discrimination by the carbamate moiety.

The significantly diminished enantioselectivity observed for tripeptide **SA2** as compared to dipeptide **SA1** is a consequence of the spatially more extended and conformationally flexible backbone. The (*all-S*)-enanti-

omer of **SA1** appears to provide ideal structural properties in terms of size as well as spatial disctance between the carboxylic group and the 3,5-dinitrobenzoyl function to enable simultaneous ion-pairing, hydrogen bonding, and $\pi-\pi$-interaction with **SO1**. Evidently, the insertion of an additional alanine unit compromises this ideal situation, weakening or even disrupting these selector-selectand interactions for (*all-S*)-**SA2**. Chromatographically, this effect should lead to a diminished overall binding energy for (*all-S*)-**SA2** relative to (*all-S*)-**SA1**, which is fully consistent with the observed retention behavior.

4. Experimental Section

4.1. Synthesis of 6′-Neopentoxy-9-*O-tert*-butylcarbamoylcinchonidine (SO1) and the Corresponding Chiral Stationary Phase (CSP1). 6′-Neopentoxy-9-*O-tert*-butylcarbamoylcinchonidine was prepared from *tert*-butylisocyanate and 6′-neopentoxycinchonidine, which in turn was synthesized from cupreine and neopentylbromide, as described in a recent publication.[12] **CSP1** was prepared by coupling **SO1** to mercaptopropyl-modified silica as decribed elsewhere.[3] The selector loading on the chiral stationary phase was calculated by using its nitrogen content determined by CHN analysis and found to be 0.24 mmol·g^{-1}.

4.2. Synthesis of the (*all-R*)- and (*all-S*)-Enantiomers of DNB-Ala$_2$ (SA1) and DNB-Ala$_3$ (SA2). All peptide enantiomers ((*all-R*)- and (*all-S*)-Ala-Ala and (*all-R*)- and (*all-S*)-Ala-Ala-Ala) were purchased from Bachem (Bubendorf, Switzerland). The peptides and a 2-fold molar excess of sodium hydrogencarbonate were dissolved in water and a 1.2-fold molar excess of 3,5-dinitrobenzoyloxysuccinimide (prepared from 3,5-dinitrobenzoyl chloride and hydroxysuccinimide by Hünig base coupling) was added. The resulting suspension was stirred at ambient temperature until a clear yellow solution was obtained (minimum 48 h). To remove the 3,5-dinitrobenzoic acid byproduct the reaction solutions were purified by preparative HPLC, using a *tert*-butylcarbamoylquinidine based chiral stationary phase (Chiral-AX QD-1, Bischoff Chromatography, Leonberg, Germany) and an 80/20 mixture of methanol/1 M aqueous ammonium acetate (0.5 M for (*all-R*)-Ala$_3$) adjusted to an apparent pH (pH$_a$) of 6.0 with acetic acid as the mobile phase. The fractions containing the products were pooled, and the solutions were concentrated on a rotavapor, acidified with hydrochloric acid (pH < 2) and extracted three times with 5 mL ethyl acetate. The combined organic layers were dried with $MgSO_4$ and the solvents were then removed with a stream of nitrogen, yielding yellow oils. Recrystallization with chloroform gave off-white powders. Purity was checked by HPLC and found to be >99% and 100% ee for all four products.

4.3. HPLC Enantiomer Separations. The chromatographic enantioselectivities α for the (*all-R*)/(*all-S*) enantiomers of *N*-3,5-dinitrobenzoylated alanine and di- and trialanine peptides (N-protection was carried out according to ref 5) were measured by HPLC, using a 150 × 4 mm i.d. column packed with the **CSP1**. The mobile phase consisted of a mixture of 80% methanol and 20% 0.5 M aqueous ammonium acetate, which was then adjusted to pH$_a$ 6.0 with acetic acid. A flow rate of 1 mL·min^{-1} was employed and the column was thermostated at 25 °C. Sample solutions (50 μL of 1 mg·mL^{-1}) were injected. UV detection was performed at 254 nm.

4.4. NMR Experiments. The monohydrochloride of **SO1** was prepared by first adding an excess of methanolic hydrogen chloride to **SO1** and subsequently evaporating the solvent to yield SO1·2HCl. To this dihydrochloride an equivalent amount of **SO1** was added, the solvent was evaporated, and the obtained **SO1·HCl** was dried in vacuo. The sodium salts of **SA1** and **SA2** were prepared by adding equivalent amounts of methanolic sodium methoxide, evaporating the solvent, and drying the resulting products in vacuo.

All compounds (free and ionized forms of the selector and the selectands) were dissolved in methanol-d_4 to give 20 mM solutions. For the complexes of **SO1** and the individual enantiomers of **SA1** and **SA2**, respectively, the single compounds were dissolved in methanol-d_4 and mixed in various ratios for the measurements of the complexation stoichiometry (Job plots) and in 1:1 ratio for the determination of the complexation-induced shifts and the intermolecular NOEs. Signal assignment of the ^{1}H NMR spectra of **SO1**, **SO1·HCl**, **SA1**, **SA2**, and the four complexes was achieved by the help of ^{1}H−^{1}H correlation (COSY), ^{1}H−^{13}C heteronuclear single quantum coherence (HSQC), and nuclear Overhauser enhancement (NOESY) spectroscopy.

The NMR spectra for the Job plot measurements were recorded on a 400-MHz spectrometer, while all other spectra were recorded on a 600-MHz spectrometer equipped with a 5-mm triple probe (^{1}H, ^{13}C, broadband) and *x*,*y*,*z*-gradients, at frequencies of 600.13 MHz for ^{1}H and 150.90 MHz for ^{13}C. The following experiments were performed at a temperature of 300 K: ^{1}H NMR (16 scans, sweep width 6100 Hz); ^{13}C NMR with the attached proton test sequence (5000 scans on average, sweep width 33 000 Hz, power-gated proton decoupling during acquisition with WALTZ-16); double quantum filtered correlation spectroscopy (DQF-COSY) with pulsed field gradient coherence selection according to the scheme of Davis et al.[27] (2048 data points in f_2, 256 data points in f_1, 16 scans, sweep width 6100 Hz, 1 ms sine-shaped gradient pulses with 20% maximum amplitude, absorption mode in f_1 using time proportional phase increments (TPPI)); NOESY (2048 data points in f_2, 256 data points in f_1, 64 scans, sweep width 6100 Hz, 800 ms mixing time, absorption mode in f_1 using TPPI); sensitivity enhanced ^{1}H−^{13}C HSQC with echo/anti-echo selection[28,29] (1024 data points in f_2, 256 data points in f_1, 16 scans, sweep width in f_2 6100 Hz, sweep width in f_1 25 600 Hz, 1 ms sine-shaped gradient pulses with 80% maximum amplitude, adiabatic ^{13}C decoupling during acquisition using a 1.5 ms CHIRP[30] pulse).

Processing was carried out as follows: All two-dimensional spectra were zero filled, doubling the data points in the direct dimension, and in the indirect dimension data points were extended two times by linear prediction forward using 64 coefficients. In both dimensions, the data were multiplied with a 90° shifted square sine window function and the spectra were phase-corrected to absorption mode.

4.5. Computational Methods. Conformational analyses, molecular mechanics geometry optimization, and molecular dynamics simulations were done with MacroModel 7.1.[31] The GB/SA continuum model[32] for solvent was used throughout. Conformation searching was done by using the grid search method.[33] Energy minimization was done by using the AMBER* force field with no cutoff of any kind invoked and implementing a conjugate gradient minimizer, using MacroModel's default convergence criteria. The molecular simulations were done by using the stochastic dynamics method to simulate the random collisions with solvent as well as solvent

(27) Davis, A. L.; Laue, E. D.; Keeler, J.; Moskau, D.; Lohman, J. *J. Magn. Reson.* **1991**, *94*, 637−644.
(28) Kay, E. L.; Keifer, P.; Saarinen, T. *J. Am. Chem. Soc.* **1992**, *114*, 10663−10665.
(29) Schleucher, J.; Schwendinger, M.; Sattler, M.; Schmidt, P.; Schedletzky, O.; Glaser, S. J.; Sørensen, O. W.; Griesinger, C. *J. Biomol. NMR* **1994**, *4*, 301−306.
(30) Böhlen, J. M.; Bodenhausen, G. *J. Magn. Reson. A* **1993**, *102*, 293−301.
(31) Mohamadi, F.; Richards, N. G. J.; Guida, W. C.; Liskamp, R.; Lipton, M.; Caufield, C.; Chang, G.; Hendrickson, T.; Still, W. C. *J. Comput. Chem.* **1990**, *11*, 440−467.
(32) Still, W. C.; Tempczyk, A.; Hawley, R. C.; Hendrickson, T. *J. Am. Chem. Soc.* **1990**, *112*, 6127−6129.
(33) Leach, A. In *Reviews in Computational Chemistry*; Lipkowitz, K. B., Boyd, D. B., Eds.; VCH: Weinheim, Germany, 1991; Vol. 2, pp 1−47.

friction forces.[34] The time step used in the numerical integration of Newton's equations was 1 fs. Initial geometries for the binary complexes were based on a crystal structure of **SO1** with 3,5-dinitrobenzoyl-(*S*)-leucyl-(*S*)-leucine.[35] By using those atomic coordinates, the structure of (*all-S*)-**SA1** was generated by modifying the leucine groups to alanine groups. The complex of (*all-R*)-**SA1** was then obtained from that structure by inverting the stereochemistries at the analyte's stereogenic centers. This was done by swapping the hydrogen and the methyl group on each stereogenic center so as to preserve the salt bridge and the $\pi-\pi$-stacking. These structures were then geometry optimized before the simulation warm-up and equilibration protocol. For **SA2** we inserted, de novo, an additional alanine group into the structure of (*all-S*)-**SA1**. The stereocenters of that structure were inverted as above to generate (*all-R*)-**SA2**. These structures were also geometry optimized prior to the simulation warm-up and equilibration. A warm-up protocol beginning from 0 to 298 K was done over a time of 5 ps. The system was then equilibrated for an additional 100 ps and then a production run of 1000 ps was carried out. This heating−equilibration−simulation protocol was used for all complexes described in this paper. Details of the methodology for simulating selector-selectand interactions in chromatography can be found in a previous paper.[36] Structures were sampled uniformly during 1-ns simulations and saved to disk for postprocessing (10 000 total structures for each diastereomeric complex). Post-simulation analysis of the SD trajectories was performed with an in-house program *anout*, which computes, among other properties, intermolecular energies and the center-of-mass (COM) positions of one molecule relative to another.[25]

Acknowledgment. This work was carried out by grants from the Austrian Science Fund (project no. P14179-CHE, N.M., W.L.), the National Science Foundation (CHE-9982888), and the Petroleum Research Fund (35172-AC4 and 39454-AC1) administered by the American Chemical Society in addition to the North Dakota Biomedical Research Infrastructure Network (K.B.L.). C.C. thanks the Austrian Academy of Sciences for supporting his work by a Ph.D. grant (DOC-Stipendium).

Supporting Information Available: Figures showing the Job plots of selector−selectand complexes, the NOESY spectra of all four complexes, the trajectories for all four complexes, the distributions of the intermolecular energies for the **SA2** complexes, and the distributions of the intermolecular fragment energies for all four complexes. This material is available free of charge via the Internet at http://pubs.acs.org.

JO0346914

(34) Gunsteren, W. F. v.; Berendsen, H. J. C. *Mol. Simul.* **1988**, *1*, 173−185.

(35) Unpublished data.

(36) Lipkowitz, K. B. *Acc. Chem. Res.* **2000**, *33*, 555−562.